Penerbit Akademia Baru

Malaysian Journal on Composites Science and Manufacturing

Journal homepage:

https://akademiabaru.com/submit/index.php/mjcsm
ISSN: 2716-6945

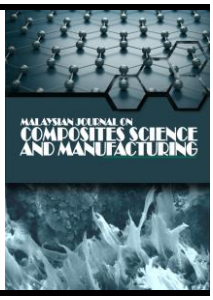

Composite Hydraulic Integration: A New Step Toward Lightweight Hydraulic Robots

M. El Asswad[1], A. Abdellatif[2,*], Maya Sleiman[3], K. Khalil[4], S. Alfayad[3]

[1] Capgemini-147 Quai du Président Roosevelt, 92130 Issy-les-Moulineaux-France, France
[2] Mechanical Engineering Department, Arab Academy for Science, Technology and Maritime Transport, Sheraton branch, 11736 Cairo, Egypt
[3] IBISC, Université d'Évry Paris-Saclay, 91020 Evry, France
[4] ECAM-Rennes, Campus de Ker-Lann, 2 Ctr. Antoine de Saint-Exupéry, 35170 Bruz, France

ARTICLE INFO

Article history:
Received 27 October 2024
Received in revised form 12 March 2025
Accepted 17 March 2025
Available online 30 March 2025

Keywords:
Hydraulic integration; Humanoid robots; Robotic arm; Assistive devices; Composite materials; Additive manufacturing

ABSTRACT

Normally, the use of hydraulics in humanoid robots is limited due to their design complexity, heavy weight, and high cost. This paper presents a new methodology for developing hydraulic integrated robotics system with lightweight, high strength, shorter production time and lower cost. This is achieved by combining the additive manufacturing of thermoplastic polymers and the simple forming of strong random fiber composites. A new methodology for fabrication of complex hydraulic integrated parts is explained in detail. The robotic arm of the humanoid hydraulic robot HYDROïD is chosen for implementing the new technique, specifically, the elbow lower part. A theoretical study for different possible 3D printing and reinforcement materials is presented. Then, an optimization method is presented to select the 3D-printed polymer material, the composite, the adequate sizes, and dimensions of the new arm part. Experimental validation and testing of the new part are presented. Moreover, PID gain scheduling controller (PID-GSC) is applied on the robotic arm during validation. The achieved results have shown that the new technique has led to significant weight reduction in the arm components to about 60% of the initial weight with a pressure tolerance of 150 bar. In addition, position tracking has been achieved successfully. Hence, the new attained solution has proved its worthiness with much lower cost and simple fabrication procedures.

1. Introduction

The development of humanoid robots has become a major focus of technological research in recent years [1]. One of the important aspects of humanoid research is the method of actuation. The types of actuation for humanoids are mainly hydraulic or electric actuation. Normally, hydraulic actuation is a less preferred option due to its heavy components, high initial cost, and possibility of oil leakage. However, hydraulic power provides high power density, high intermitted force, high

* *Corresponding author.*
E-mail address: a_abdellatif@aast.edu

https://doi.org/10.37934/mjcsm.16.1.150166

stiffness, and high actuation response [2]. Thus, research has been ongoing on using hydraulic power in humanoids and to try to overcome its challenges [3].

Hydraulic integration is a new technology where the hydraulic system pipes are replaced by internal hydraulic passages through the system components. It is used in several application domains such as aeronautics, hydraulic power system and robotics systems [4]. Recently, researchers are considering this technology due to its advantages. First, this technology eliminates the excessive weights due to the piping system, by integrating the hydraulic passages in the mechanical parts. Moreover, it reduces the assembly and maintenance time when building the mechanism. In addition, because the limitations related to the pipes length is removed, robotics systems gain more flexibility in the joint motions, eliminating the pipes stiffness, which relatively increases the bandwidth of the actuator and facilitates the robot control. Incidentally, and especially talking about humanoid robots, robot structural organization is closer to the human one. Finally, eliminating the piping systems reduces the leakage in the hydraulic system.

Researchers proposed hydraulic integration using additive manufacturing to fabricate a manifold for Aircraft landing gears applications [5]. Boston Dynamics has recently developed hose-less components for their humanoid robot Atlas [6]. Barasuol et al. has a successful experience in developing lightweight hydraulic integrated robotic parts [7]. The components, in both previous cases, are manufactured using additive manufacturing of metals. Moreover, researchers in [8] and [9] have used hydraulic integrated manifold for developing a compact hydraulic power system. In addition, WLR robot team [10] has developed an integrated and optimized hydraulic wheel-legged hybrid robot (WLR), with innovative and enhanced hydraulic integrated design. As for the robot at hand, HYDROïD robot [11], the authors used hydraulic integration in several components of the robot. They used advanced machining procedures such as electric discharging process to manufacture the oil internal passages inside metallic components of the robot.

Despite these successful applications, hydraulic integration still suffers from several negative points related to cost, process complexity, manufacturing difficulties, mechanism weight and development time. The electric discharge machining process of hydraulic integrated components is a complex process and has some bad effects on the material properties of the parts. Due to the high imposed temperature [12], it could inherently affect the mechanical properties of the produced part by inducing residual stresses, which need heat relief after the fabrication process. In addition, for parts with several internal passages, it is expensive and consumes a lot of time. Moreover, the component needs laser point soldering to close the undesirable opening occurring in hydraulic passages.

Normally, additive manufacturing of metals can be realized with one of the two following types of processes: selective laser sintering (SLS) or electron beam melting (EBM). EBM has several technical drawbacks such as a high cost, low accuracy, and geometric limitations. SLS process has a long building time, which increases the cost of manufacturing. In theory, this procedure requires the design to have a constant cross section and it makes it very difficult to design parts with complex details. Note that in both metal additive manufacturing procedures an important post heat treatment is required to relieve the parts from the residual stresses induced by the manufacturing process. Furthermore, removing the powder metallic support in very small spaces is very difficult and hard to achieve. Furthermore, using metals in the all the described methodologies process is adding weight to the mechanisms. Finally, plastics additive manufacturing cannot be a standalone solution due to plastics' low strength which couldn't support the high induced internal pressures [13].

This calls for the development of a new methodology to achieve hydraulic integration and overcome the drawbacks of the previously mentioned methodologies. The methodology proposed in this paper combines additive manufacturing with the classical procedures of composite materials

forming. It solves the complexity related to the internal passages using the additive manufacturing of adaptive thermoplastic polymers. By this way, the printing cost is a fraction of the original cost of printing metals and does not need complex post curing processes. To acquire the necessary strength for the thermoplastic printed internal passages, random fiber composites are added between the spaces surrounding all printed passages and forming a multi-layer material. The choice of random composites is justified by the forming process simplicity and their low cost. This methodology and its application to the arm of HYDROïD robot is introduced in this paper.

This paper is divided into 5 sections excluding the introduction. It starts by presenting the complexity of present hydraulic integration processes. Then, it describes the challenges and the new proposed solution to overcome the drawbacks of conventional processes. In the fourth section, it explains the theories & formulations used to calculate different design parameters & optimize materials' selection. Later in the 5th section, we carried out different experimental validations, to confirm process reliability and conclude its different advantages and shortcomings. This paper ends with a conclusion which summaries paperwork in one hand and open horizons for future work in another hand.

2. Problem Statement

HYDROïD (HYDraulic andROïD) is a full-size humanoid robot that aims to contribute to improving our understanding of the phenomena of locomotion and manipulation of humans. Humanoids with hydraulic actuation can achieve hard and useful tasks and replace human in disaster environment. Moreover, a new integrated hydraulic actuation method was proposed and implemented on HYDROïD. The goal is to eliminate all external pipes and replace them with integrated hydraulic passages. Fluid paths is integrated internally through the mechanical structure and not externally through pipes. In other words, arteries and veins were built inside the HYDROïD body to drive hydraulic fluid like blood in human body.

The objective is to reduce the weight of HYDROïD robot, and to reach the target weight of normal adult of 1.8 m height (74.6 kg). The current prototype has a weight of 125 kg, when the targeted weight is 75 kg [14], which means that it is required to diminish the robot weight by 50 kg. The robot 3D CAD design is shown in Figure 1a.

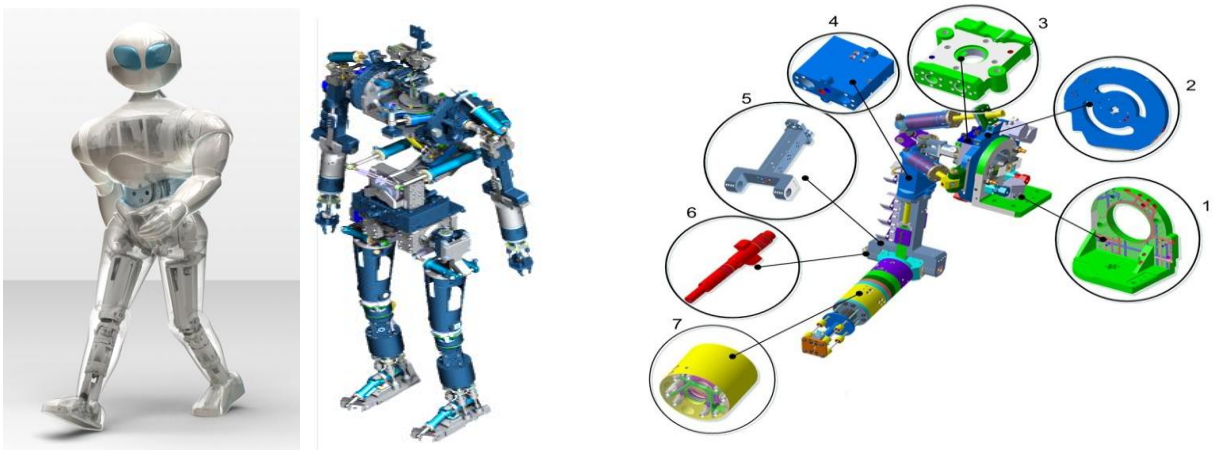

(a) (b)

Fig. 1. a) HYDROïD robot CAD 3D model b) Overview on the arm hydraulic integrated parts masses: 1- Shoulder upper part, 2- Shoulder middle part, 3- Shoulder lower part, 4- Elbow upper part, 5- Elbow lower part, 6- Elbow axis of rotation, 7- Wrist part

HYDROïD mechanical components can be divided into 4 groups: hydraulic integrated parts (HIP), structural parts (SP), hydraulic cylinders (HC) and commercial parts (CP). Hydraulic integrated parts compose about 60 % of the arms weight, 70% of the torso weight and 35% of the legs weight. Thus, the hydraulic integrated parts (HIP) compose about 50% of the robot weight. HIP supports internal pressures and piston forces. Figure 1b shows an example of the hydraulic integrated parts in the arms.

3. Challenges & Proposed Solution

Before explaining the proposed solution, it is important to explain in detail the challenges of manufacturing hydraulic integrated parts. The mechanical part in Figure 2a acts as a manifold for 3 valves which are responsible for controlling the oil flow to the wrist actuators. It is fabricated of aluminum, and it weighs 900 g.

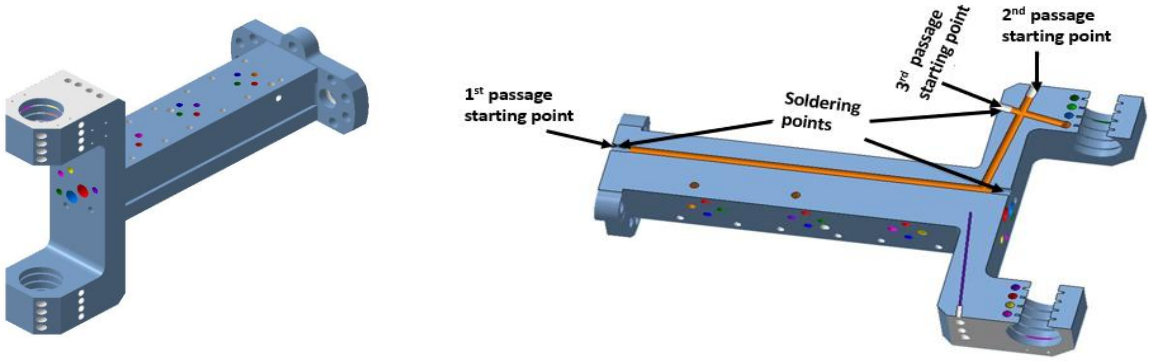

(a) (b)

Fig. 2. a) Elbow lower part (part No.5) of hydraulic integrated parts of the arm b) Illustration of the fabrication complexity of oil passages

The difficulty in fabricating this part is its complexity. This part contains 14 internal hydraulic passages, in which some of them are 160 mm long. To connect two perpendicular passages, the first passage is opened from the first plane, then the second passage is opened from the perpendicular plane and finally welding is used to close the starting points of each passage. The welding used to close the two ends of these small passages is laser welding [15]. This process has a high cost and needs a long time especially when considering 14 passages. Figure 2b illustrates how small the passage diameter is compared to its length (3.5 mm diameter compared to 166 mm length). This passage is connected to other passages, which makes it an expensive, & a complex process. Therefore, it was fabricated using electrochemical machining process [16], which needs post surface treatment.

Thus, HIP fabrication has two main challenges: hydraulic integration and high strength with lightweight. The hydraulic integration is solved using the technology of 3D printing of non-metal materials. First, several lightweight printable materials are chosen. Second, these materials are arranged according to their mechanical properties. Third, the best material is chosen according to the value of a cost function, which contains all the different parameters of the elected materials. Moreover, design optimization is performed to calculate minimum distance necessary to reinforcement. This is using multi-layer tubes theory. The internal layer is the 3D-printed passage, while the external layer is the composite material. Finally, a study was carried out to choose the characteristics of the random fiber reinforcement, according to the load cases, and according to the

necessary weight reduction. In that way, discontinuous random fiber theory is applied, to best choose the fiber needed, the resin needed and the necessary fiber volume for reinforcement.

After printing the part, all the support inside the passages is removed using air pressure and a certain basic finish is done to remove the support marks on the outer surfaces by using smoothing and polishing. Then, the random composite reinforcement is added according to the calculated quantity, and it is left at rest at room temperature. Once the composite has cooled down to reach the necessary properties, the surface mounting the servo-valves should be smoothed, using post smoothing process for 3D-printed components. The second surface requiring high quality is the surface for the oil inlet and oil outlet ports, connected to the rest of the arm. Then, it is time to add some accessories such as inserts for servo-valves mounting and the part is ready. The overall procedure is summarized in Figure 3. The advantages of this process are its simplicity and the short time for manufacturing. This way, technical problems are reduced, and the passages are totally separated.

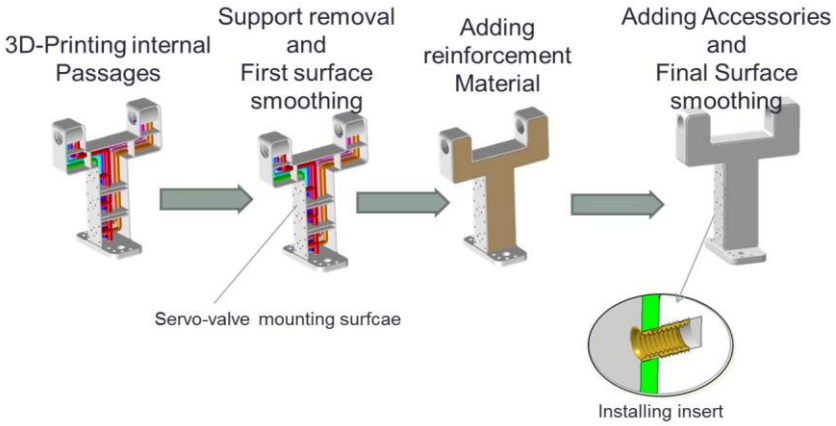

Fig. 3. Illustration of the procedure steps starting from internal passages printing ending with adding the accessories

4. Material Selection and Design Formulation

4.1 Theoretical Study of the 3D Printed Material

In this study, we limited our choices with the polymers and polymers filled with fibers due to their simple printing process. In general, three methods are used to print polymers: Stereolithography, material extrusion and powder bed fusion. Material extrusion materials, generally, includes ABS, polycarbonate, polystyrene and ULTEM, while powder bed fusion includes polyamide, polyamide filled with glass fiber and Allumide and finally Stereolithography includes mainly epoxy. From each method, most functional materials in terms of strength are chosen.

Moreover, each of the 3D-printing materials is characterized by its density, price, precision, strength and working temperature. Thus, the best choice is the material with the lowest prices P_r, lowest density ρ, the highest precision μ, the highest strength R and the highest working temperature T_{max}. Accordingly, the cost function for the ranking of the materials F is defined in Eq. (1).

$$F = \frac{RT_{max}}{P_r \rho \mu} \quad (1)$$

This function will be used to find the best material to be used to 3D-print the internal passages.

4.2 Reinforcement Material

The criteria used to compare the different random fiber composites reinforcement are the strength σ_c, the density ρ and the price P_r. The modified rule of mixtures for random fiber, which takes into consideration the length of the fiber l, the dispersion of the fiber and the shear strength of the matrix τ_m, is employed. It also defines the critical length of the fiber necessary for reinforcement l_c. For $l < l_c$ [17], the strength of the composite can be calculated as Eq. (2).

$$\sigma_c = \nu_f \frac{l\tau_c}{d} + (1 - \nu_f)\sigma_m \quad (2)$$

Where σ_c is the strength of the composite and ν_f is the carbon volumetric ratio. The shear strength of the matrix τ_m is approximated to be half the tensile strength of the matrix σ_m . For the second case where $l > l_c$, Eq. (3) is used to calculate the composite strength.

$$\sigma_c = \nu_f \sigma_f \left(1 - \frac{l_c}{2d}\right) + (1 - \nu_f)\sigma_m \quad (3)$$

Where σ_f is the fiber tensile strength and d is the fiber diameter. The fiber critical length can be calculated as Eq. (4).

$$l_c = \frac{\sigma_f d}{2\tau_m} \quad (4)$$

In addition, the price P_r and the density ρ are calculated using Eq. (5) and Eq. (6).

$$P_{rc} = P_{rf}\rho_f\nu_f + P_{rm}\rho_m(1 - \nu_f) \quad (5)$$

$$\rho_c = \rho_f\nu_f + \rho_m(1 - \nu_f) \quad (6)$$

Where P_{rc} is the composite price in (euro/cm^3), P_{rf} and P_{rm} are the fiber and the matrix prices respectively in euro/g. ρ_f and ρ_m are the fiber and the matrix densities in g/cm^3. ρ_c is the composite density. Finally, the elastic modulus E_c is calculated for random fiber composite reinforcement using Eq. (7).

$$E_c = \nu_f \frac{E_f}{k} + (1 - \nu_f)E_m \quad (7)$$

Where E_f is the fiber young modulus, k is the 3D-random fiber dispersion factor and E_m is the Young's modulus matrix.

4.3 Study of the New Design

In this section, the design parameters, and their effect in the choices of the reinforcement materials are discussed. The main design parameters that affect the reinforcement material choices are the internal diametric ratio $R_i = \frac{b}{a}$ and the external diametric ratio $R_o = \frac{c}{b}$. To achieve this, the multilayer theory is applied. As shown in Figure 4, the internal layer is the 3D-printed plastic, while the external layer is the random fiber composite reinforcement.

To find the design parameters, the classical elasticity theory of multilayer thick-walled cylinder is used [14]. The different cylindrical stresses in the internal and external layers are shown in Figure 5. The elasticity material parameters of the internal and the external layers are designated as: E_i Young modulus of the internal layer (PA-GF: polyamide filled with glass fiber), ν_i the Poisson ratio of the internal layer, E_o the young modulus of the external layer and ν_o is the Poisson ratio of the external layer. Thus, due to the internal pressure P_i, an interface radial stress P_f is produced. By applying this theory, P_f can be calculated as Eq. (8).

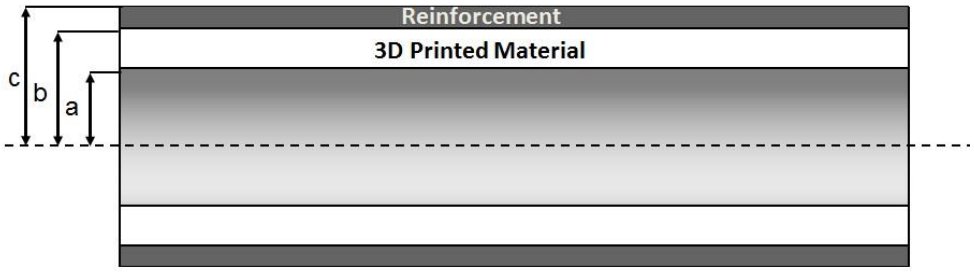

Fig. 4. Geometrical representation of the multilayer tube: (a) the internal diameter of the internal layer, (b) the internal diameter of the outer layer and (c) the outer diameter of the outer layer.

$$P_f = \frac{2P_i}{E_i(R_i^2-1)\left[\frac{1}{E_i}\left(\frac{R_i^2+1}{R_i^2-1}-\nu_i\right)+\frac{1}{E_o}\left(\frac{R_o^2+1}{R_o^2-1}+\nu_o\right)\right]} \quad (8)$$

Where $R_i = \frac{b}{a}$ and $R_o = \frac{c}{b}$ are the diametric ratio of the internal and the external layers respectively.

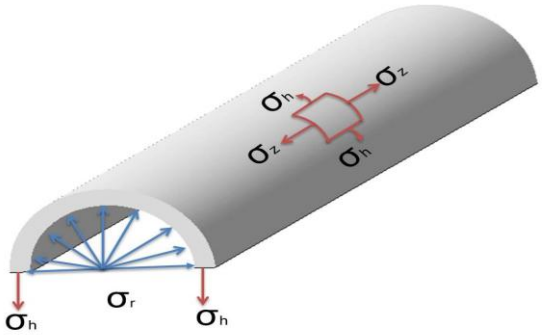

Fig. 5. Illustration of the different cylindrical stresses in the internal and external layers.

The different stresses to calculate are the hoop stresses, the maximum radial stress, and the axial stress. The hoop stresses in the internal and the external layers are calculated using Eq. (9) and Eq. (10).

$$\sigma_{hi} = \frac{P_i}{R_i^2-1}\left(1+\frac{b^2}{r^2}\right) - \frac{P_f R_o^2}{R_i^2-1}\left(1+\frac{a^2}{r^2}\right) \quad (9)$$

$$\sigma_{ho} = \frac{P_f}{R_o^2-1}\left(1+\frac{c^2}{r^2}\right) \quad (10)$$

Where r is the radius at any thickness of the cylinder wall. Eq. (9) and Eq. (10) have maximum values at r = a and r = b respectively, and the maximum internal hoop stress σ_{him} is written in Eq. (11).

$$\sigma_{him} = \frac{P_i}{R_i^2-1}(1 + R_i^2) - \frac{2P_f R_o^2}{R_i^2-1} \tag{11}$$

Moreover, the maximum radial stress σ_{rim} at the internal layer is calculated using the Lamie's equations for the theory of thick cylinder with internal pressure P_i and external pressure P_f, and is written as Eq. (12).

$$\sigma_{rim} = -\frac{P_i(R_i^2-1)+2R_i^2 P_f}{R_i^2-1} \tag{12}$$

The axial stress σ_{zim} is calculated in Eq. (13).

$$\sigma_{zim} = \frac{P_i - R_i^2 P_f}{R_i^2-1} \tag{13}$$

Finally, we deduce the maximum von Mises stress at the internal layer in Eq. (14).

$$\sigma_{vim} = \sqrt{\frac{(\sigma_{him}-\sigma_{rim})^2+(\sigma_{him}-\sigma_{zim})^2+(\sigma_{rim}-\sigma_{zim})^2}{2}} \tag{14}$$

Thereafter, the stresses in the external layer (reinforcement composite) are calculated using Lamie 's equation for a thick cylinder under internal pressure P_f. There are 3 main stresses: radial stress, the hoop stress, and the axial stress σ_{rom}, σ_{hom} and σ_{zom}. These stresses are used to find the von Mises stress at the external layer of the multilayer tube. They are all stated in Eq. (15), Eq. (16), Eq. (17) and Eq. (18) respectively.

$$\sigma_{rom} = -P_f \tag{15}$$

$$\sigma_{hom} = \frac{P_f(R_o^2+1)}{R_o^2-1} \tag{16}$$

$$\sigma_{zom} = -\frac{-P_f R_o^2}{R_o^2-1} \tag{17}$$

$$\sigma_{vom} = \sqrt{\frac{(\sigma_{hom}-\sigma_{rom})^2+(\sigma_{hom}-\sigma_{zom})^2+(\sigma_{rom}-\sigma_{zom})^2}{2}} \tag{18}$$

The maximum von Mises stress at the internal layer σ_{vim} should be smaller than its tensile strength R and the maximum von mises stress at the external layer σ_{vom} should be smaller than its tensile strength σ_c. Thus, two factors f_1 and f_2 are defined in Eq. (19) and Eq. (20).

$$f_1 = \frac{\sigma_{vim}}{R} \tag{19}$$

$$f_2 = \frac{\sigma_{vom}}{\sigma_c} \tag{20}$$

For the best choices of materials and design factors, f_1 and f_2 are the constraints that should have the least possible values. In addition, the chosen material should have the lowest price P_{rc} and the lowest density ρ_c. Accordingly, function H is deduced in Eq. (21).

$$H = \frac{1}{\rho_c P_{rc} \sqrt{f_1 f_2}} \tag{21}$$

The available 3D-printed materials and reinforcement materials are provided in Tables 1 and 2. The numerical values have been obtained from references [18], [19], and [20].

Table 1
Table of comparison of different selected 3D-printing materials
(PA-GF: Polyamide filled with glass, ULTEM: polyetherimide based material)

Material	PA-GF	Allumide	ULTEM	Epoxy
ρ (kg/m^3)	1250	1350	1340	1100
P_r (euro/cm^3)	0.5	0.7	4.7	4.3
μ (%)	0.3	0.3	0.1	0.2
R(Mpa)	51	48	72	32
$T_{max}°C$	110	130	153	61

Table 2
Different properties of the selected reinforcement fibers and resins (CF: Carbon fiber, GF: Glass fiber)

Material	CF	GF	Epoxy	Polyester	Polyurethane
ρ (kg/m^3)	1800	2590	1120	1150	1100
σ (MPa)	3150	2420	65	60	50
E (GPa)	200	72	2.6	4	2.2
d (μm)	7.5	16	-	-	-
l (μm)	100	230	-	-	-
P_r (euro/g)	0.02	0.02	0.012	0.01	0.02

4.4 Results and Discussion

To find out the best material available for 3D-printing in Table 1, the ranking method is used for election. For example, according to its tensile strength, ULTEM is ranked as number 1 while epoxy is ranked as number 4. In contrary, Epoxy is ranked number 1 according to its density while Allumide is ranked as number 4. The ranking process is very complex and can depend in many factors that can be weighted differently according to the application of the designed robot. Here, we deduced to give all factors the same weight, according to the cost function F (Eq. (1)). According to the obtained results, PA-GF has the priority while epoxy has the least priority.

Table 3
Ranking of the selected 3D-printing materials

Material	PA-GF	Allumide	ULTEM	Epoxy
ρ (kg/m^3)	2	4	3	1
P_r (euro/cm^3)	1	2	4	3
μ (%)	3	3	1	2
R(MPa)	2	3	1	4
$T_{max}°C$	3	2	1	4
F	1	2	3	4
Priority	1	3	2	4

On the other hand, choosing the random fiber reinforcement will be more difficult due to the dependence of the material properties in the fiber aspect ratio v. The available fibers and resins can be combined into 6 different composites: CF/Epoxy, CF/Polyester, CF/Polyurethane, GF/Epoxy, GF/Polyester and GF/Polyurethane. According to Table 4, l < l_c for the 6 types of composites. Thus, only the theory of discontinuous random fiber is applicable in these cases.

Table 4
Comparison of the length and the critical length for each type of the random composite

Material	l (μm)	l_c (μm)
CF/Epoxy	100	363
CF/Polyester	100	394
CF/Polyurethane	100	427
GF/Epoxy	230	596
GF/Polyester	230	2645
GF/Polyurethane	230	774

To construct the priority table of selection for the different types of reinforcement, the function H is plotted against the fiber aspect ratio ν_f and the external diameter ratio R_o. Figure 6 presents the trends of function H with respect to the fiber aspect ratio ν_f and the diametric ratio of the outer layer R_o for CF/Epoxy. The graph is divided into 3 main regions: region 2 of acceptable values, region 3 of favorable values and region of 1 non-useful values. In the region of the acceptable values, the fiber aspect ratio ranges from 0.1 for a diametric ratio of 2 to 0.5 to a diametric ratio of 1.5. In the favorable region, ν_f ranges from 0.225 for R_o equals to 1.75, to 0.5 for R_o equals to 2.25. The ultimate value for function H is 6.2. Table 5 summarizes the results of simulations in the 6 different 3D-curves. Now ranking table is achieved according to the values of ν_f, R_o and H at the favorable region for the 6 different composites.

Table 5
Comparison of the obtained results of the simulated function H for different composites reinforcements

Material	Acceptable values		Favourable values		H_{cult}
	ν_f	R_o	ν_f	R_o	
CF/Epoxy	0.1-0.5	1.5-2	0.23-0.5	1.75-2.25	6.2
CF/Polyester	0.2-0.8	1.5-1.75	0.2-0.45	2-2.5	5.8
CF/Polyurethane	0.3-0.7	1.5-1.8	0.3-0.7	2.25-2.5	5
GF/Epoxy	0.3-0.6	1.6-2.4	0.35	2.5	4.25
GF/Polyester	0.5	2.25	0.2	2.15	4.5
GF/Polyurethane	0.45	1.8	0.23	2.5	3.25

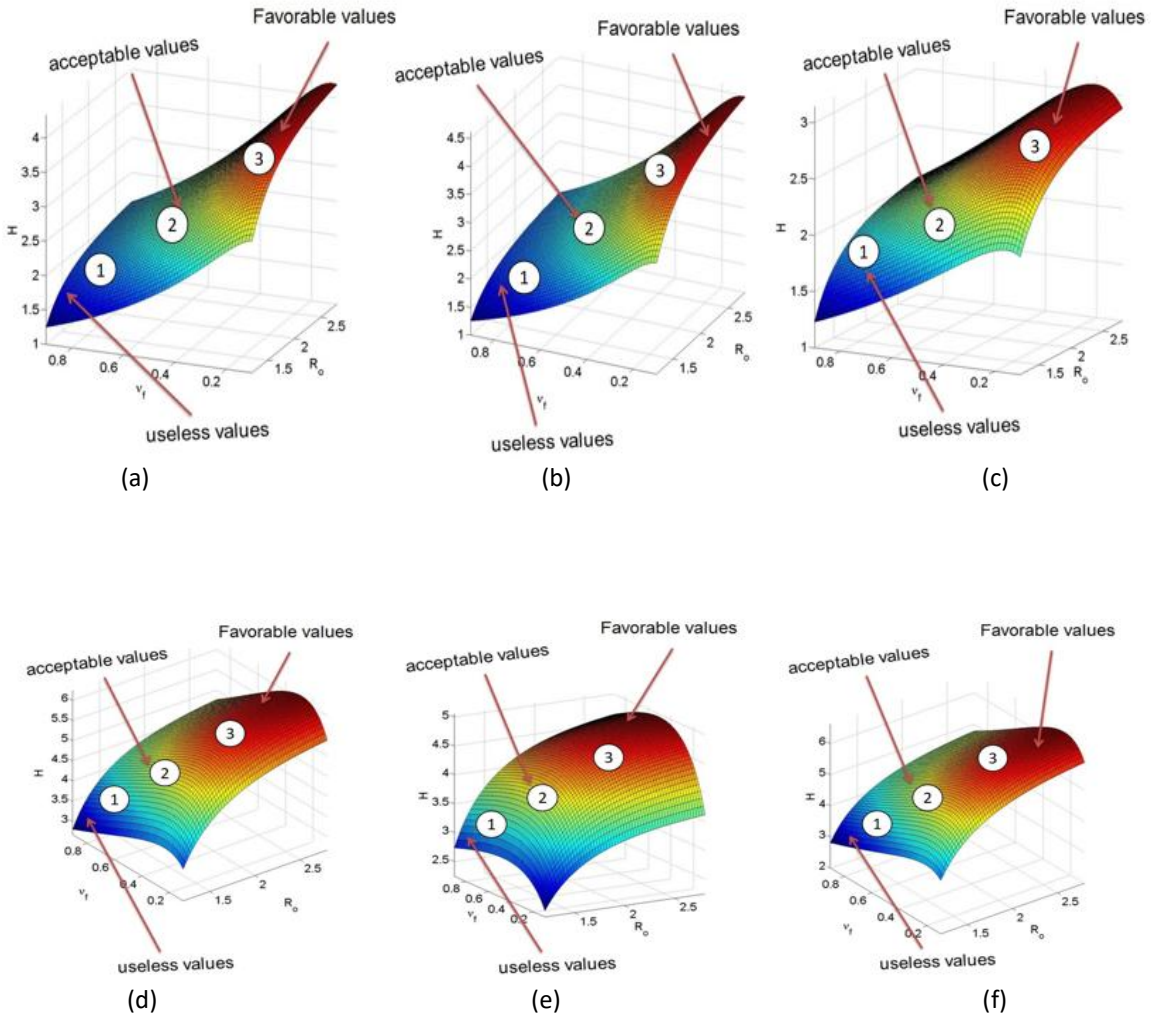

Fig. 6. Simulation results of function H for different materials like: (a)CF/Epoxy, (b)CF/Polyester, (c)CF/Polyurethane, (d) GF/Epoxy, (e) GF/Polyester and (f) GF/Polyurethane. Region 1 for useless values, region 2 for acceptable values and region 3 for favorable values.

The resultant ranking Table 6 shows that CF/Epoxy has the highest priority of choice while GF/Epoxy has the lowest priority of choice. Consequently, CF/Epoxy is chosen as the composite material used for reinforcement. After carrying out the optimization process and using ranking tables, the favorite aspect ratio is ν_f =0.35. The material characteristics are calculated in Table 7.

Table 6
Ranking table for the reinforcement materials

Material	ν_f	R_o	H	Total
CF/Epoxy	2	1	1	4
CF/Polyester	1	2	2	5
CF/Polyurethane	3	4	3	10
GF/Epoxy	5	4	5	13
GF/Polyester	1	3	4	8
GF/Polyurethane	2	4	6	12

Table 7
CF/Epoxy Material Properties for average favorable aspect ratio ν_f =0.35

CF/Epoxy	
σ_c (MPa)	346
ρ_c(g/cm^3)	1.35
E_c(GPa)	16

5. Experimental Validation

5.1 Samples Testing

To validate the theory of multilayer pipe, cylindrical form samples are prepared. They are composed of 2 layers: the outer layer of random carbon fiber/epoxy composite & inner layer of 3D-printed PA-GF. 9 types of specimens are fabricated and summarized in Figure 7 where D is the outer diameter of the outer layer, C is the inner diameter of the outer layer, B is the outer diameter of the inner layer and A is the inner diameter of the inner layer.

The manufacturing process started with printing PLA cylinders according to the dimensions provided in the previous figure. The moulding of the cylinders is challenging. In fact, due to the long cylinder shape (mm), the internal cylinder shifted due to the heat generated by the hardening process of the epoxy. To overcome this, the specimen was moulded by phases. At each phase, the mould was placed in front of a fan to allow it to cool. Figure 8a below shows an example specimen taking into consideration that the carbon aspect ratio is 10%. In addition, the hydraulic circuit that has been utilized in testing is shown in Figure 8b. The highest pressure among the 9 specimens was 75 bar for specimen 5.

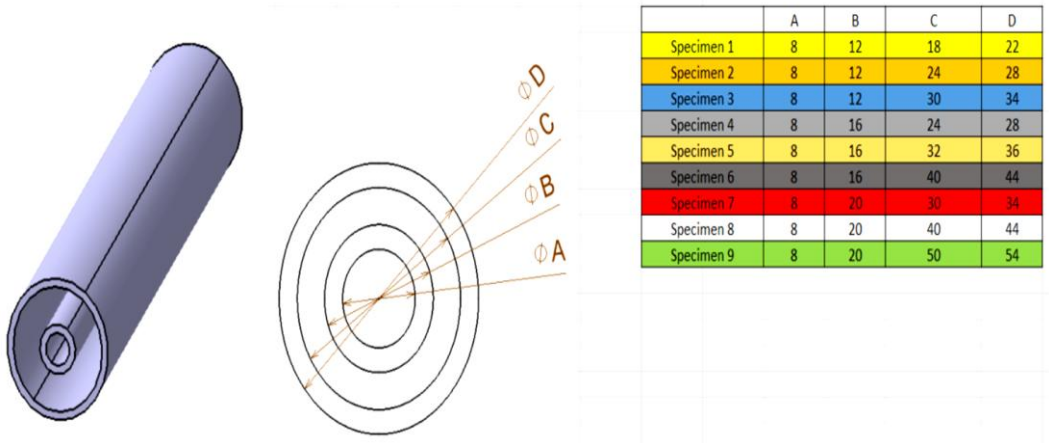

	A	B	C	D
Specimen 1	8	12	18	22
Specimen 2	8	12	24	28
Specimen 3	8	12	30	34
Specimen 4	8	16	24	28
Specimen 5	8	16	32	36
Specimen 6	8	16	40	44
Specimen 7	8	20	30	34
Specimen 8	8	20	40	44
Specimen 9	8	20	50	54

Fig. 7. The 9 fabricated samples and their diameters

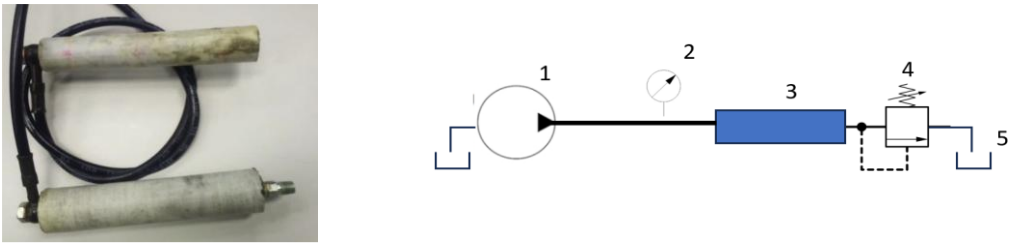

(a) (b)

Fig. 8. a) The fabricated testing samples b) The testing hydraulic circuit that contains the pump (1), pressure gauge (2), the specimen pipe (3), pressure relief valve (4) and hydraulic tank (5)

5.2 Testing of the New Elbow Lower Part

In this section, it is intended to validate the methodology by fabricating hydraulic elbow lower part using the new method and integrating it in HYDROïD arm to be exposed to the high pressure. First, the added composite should be perfectly degassed to get rid of voids using degassing chamber which increases the strength of the part. On the other hand, the mounted inserts should fit with the printed material. An applied example is the part shown in Figure 9a. The part is printed using nylon filled with glass fiber (PA-GF). There are 3 layers of internal passages, the inlet passage, the servo-valves passages, and the outlet passage.

To remove the voids from the moulded composites, a degassing chamber is used [21]. The epoxy resin filled with carbon fiber has increased by 35% (ν_f = 0.35) to provide more pressure resistance. The moulded composite is placed inside the chamber at a vacuum -0.4 mbar for 15 min, before it is added between the passages. Then, the moulded part with the composite is placed itself inside the chamber to make sure almost all the voids are eliminated. The new part is 60% lighter than the metallic part and the fabrication process is much simpler. After fabrication process ended, the manufactured part is integrated in HYDROïD robot arm for testing (Figure 9b). The arm is connected to a commercial dexterous humanoid gripper which holds a 1.5 L water bottle as a load.

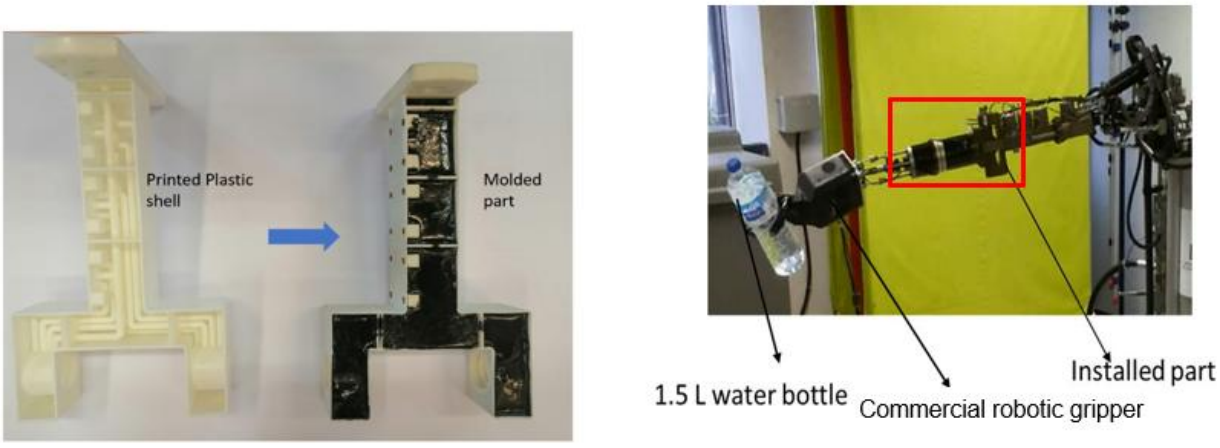

a) b)

Fig. 9. a) The upper elbow mechanical part from 3D-printing to composite moulding b) The new fabricated part (shown in red) is installed to HYDROïD robot arm for testing and validation under different pressure ranges

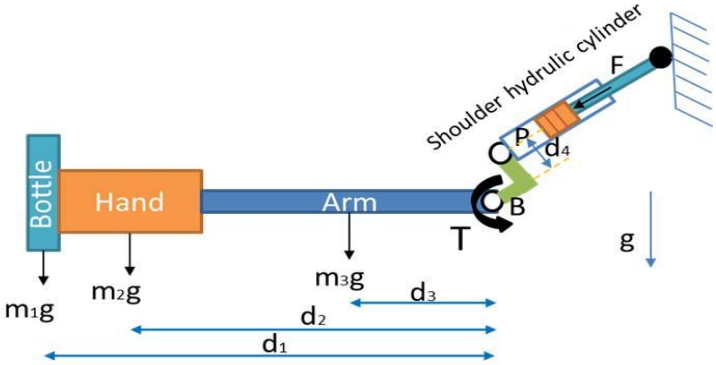

Fig. 10. Force model of the arm at the horizontal position used to calculate the maximum pressure applied at the shoulder

By considering arm lengths and weight, the numerical parameters for the robot's arm are as follows: m_1 = 1.5 kg, m_2 = 4.2 kg, m_3 = 10 kg, d_1= 1 m, d_2 = 0.7 m, d_3 = 0.3 m, d_4= 0.01 m, A_{piston}= 4.91 x 10^{-4} m^2 and g = 9.81 m/s^2). The resultant pressure is 150 bar as per Eq. (24) and Figure 10.

$$P_i = \frac{m_1 g d_1 + m_2 g d_2 + m_3 g d_3}{A_{piston} d_4} \quad (22)$$

By applying the calculated pressure and a convenient position control scheme (Figure 11), the mechanism is tested at different positions validating the strength of the fabricated component and the implemented methodology. The real consumed pressure is 160 bar, which is higher than the calculated one due to the internal friction forces in the mechanism. Thus, the new manufactured part has tolerated pressure greater than 150 bar.

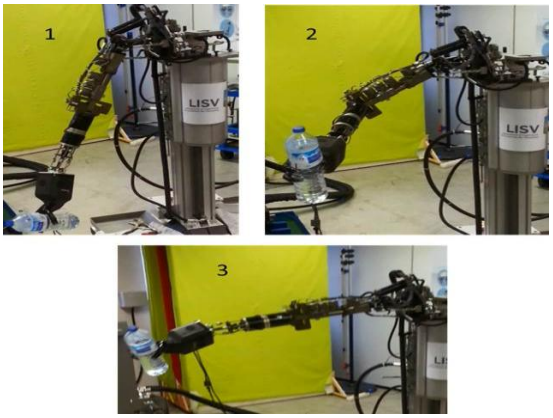

a)

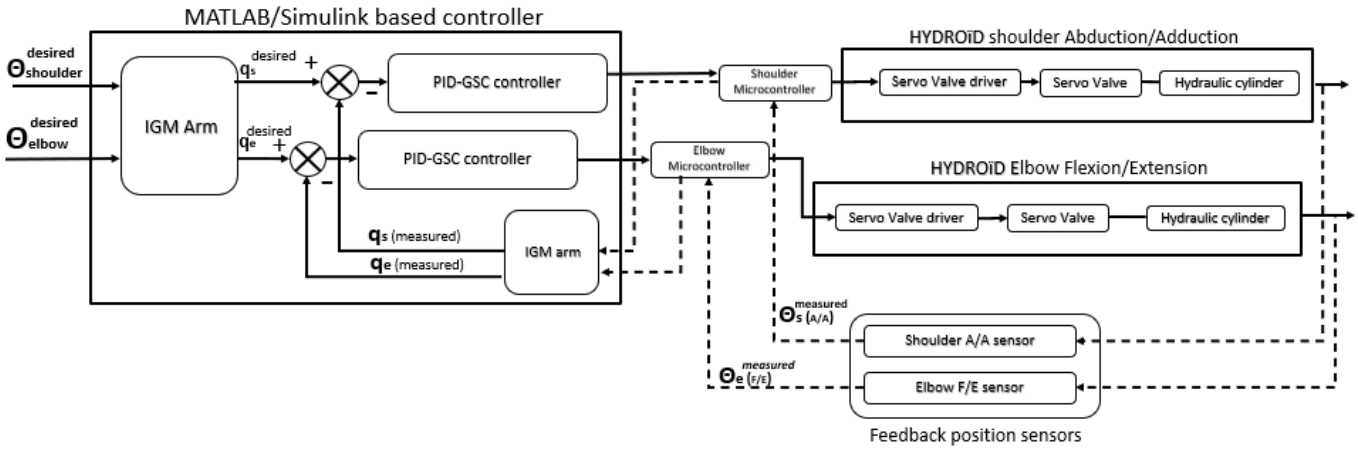

b)

Fig. 11. a) The implemented position control loop for the shoulder joint (abduction/adduction) and elbow joint (flexion/extension) b) Testing the mechanism at different positions using the implemented control model

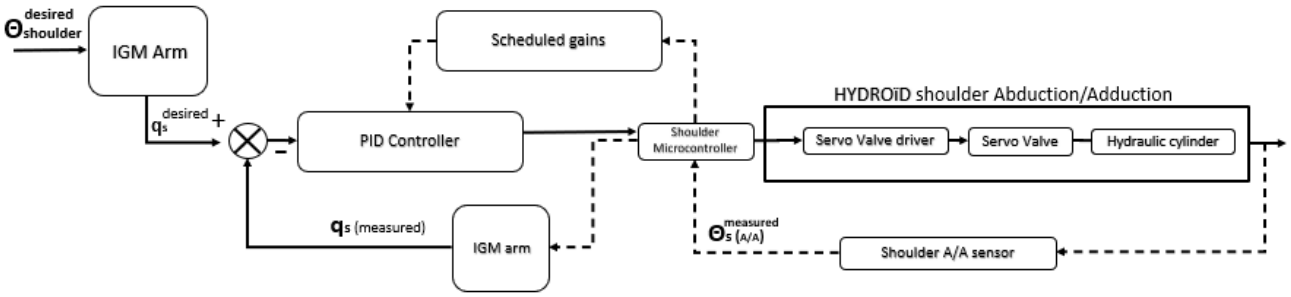

Fig. 12. The PID-GSC controller applied on shoulder Adduction/Abduction joint

The control software that is shown in the previous figure is a MATLAB/Simulink based controller [22,23]. The arm inverse geometrical model (IGM) is calculated to get the desired $\theta_{elbow}^{desired}$ and $\theta_{shoulder}^{desired}$ angles. The control methodology that has been used in PID gain scheduling controller (PID-GSC) which updates the PID gains according to a predefined schedule. It is used due to the nonlinearity of the system. A block diagram that describes this controller is shown in Figure 12. The utilized hardware for the control of the arm is shown in Table 8.

Table 8
The utilized hardware for HYDROïD robotic arm

Item Name	Technical Specifications
Personal computer	Intel core i7 with 2.8 GHz processor speed and 24 GB of RAM
Hydraulic pump	MTS 505 silent flow hydraulic group with a fixed displacement radial piston pump with P_{max} = 220 bar and Q_{max} = 20 l/min
Servo valve	MOOG 30 two stage servo valve with Q_{max} = 12 l/min and $P_{max} = 210\ bar$
Valve driver	MY502 servo valve amplifier with 24V and 15 mA power inputs
Microcontroller	Arduino Mega 2560 Rev3
Position sensor	12-bit AMS5045B contactless magnetic position sensor
Pressure sensor	4LC piezo-resistive sensor with chip in oil capability (CIO) and P_{max} = 200 bar

The experimental position response of the shoulder abduction joint rotation is shown in Figure 13. It shows the accurate tracking of the desired angle using the proposed controller. The shoulder joint desired angle is 90° while the peak consumed pressure is approximately 23 bar. The dynamic responses show the validity of the new integrated parts and the applied controller. The response maximum overshoot is 3.63%, the steady state error is 0.96° and the settling time is 110 ms.

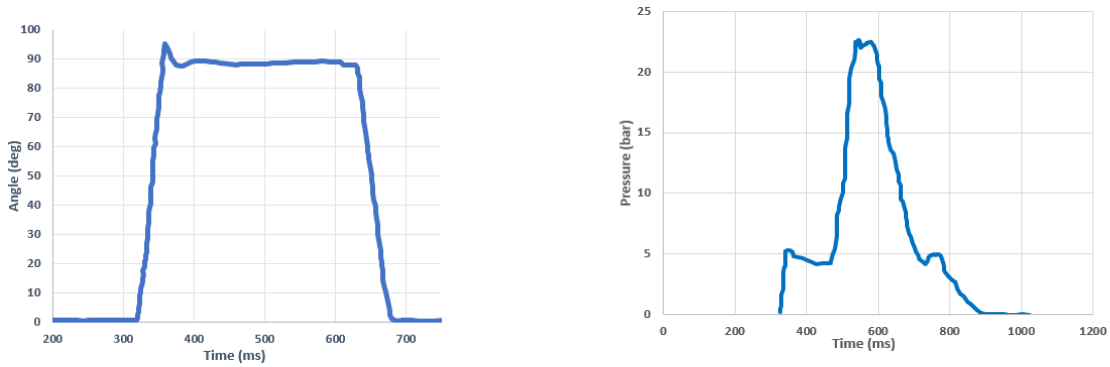

a) b)

Fig. 13. a) The output response for shoulder abduction rotation b) The consumed pressure during shoulder joint movement

6. Conclusions and Future Work

In this paper, a new methodology for fabricating hydraulic integrated robotics components was proposed. This feat is achieved by the latest additive manufacturing technologies with the classical composite materials fabrication methods. First, a ranking model was carried out to choose the appropriate additive manufacturing technology and material in one hand, and the suitable fiber/resin combination with optimized characteristics in another hand. After material selection, the design parameters were then incorporated into the model to obtain their optimum values. Meanwhile, the results of the optimization model were discussed. PA-GF material was found to be the best for 3D-printing and CF/Epoxy composite was the most suitable for reinforcement. To validate this methodology, it was applied on several specimens and on one of the complex hydraulic integrated parts of HYDROïD robot arm. Results have shown that with 10% fiber, the specimen resisted up to 75 bar. In addition, for 35%, the arm part has resisted 150 bar applied pressure, when installed in the robot arm. Gain Scheduling PID controller is applied on the robotic arm shoulder joint and the experimental responses have shown accurate tracking of the desired rotation values.

For future work, fatigue dynamic loading tests will be performed on the new composite parts. Additionally, studying the mechanical stresses from external loads will be essential and will be used to enhance the newer version of the manufactured parts. Such new composite parts can be generalized and applied to all hydraulic integrated parts of the robot. Thus, weight of the robot and the consumed pressure will be reduced significantly. Additionally, the impact of weight reduction on robot performance. Finally, a friction model should be implemented to study how oil will interact with 3D-printed parts.

Acknowledgement

This work is financially supported by the French company BIA- TURNKEY TEST SYSTEMS (BiA). The complete fieldwork has been done at the University of Versailles (UVSQ) - Paris Saclay, France.

References

[1] Halim A, Abdellatif A, Awad MI, Atia MRA. “Prediction of human gait activities using wearable sensors”, Proceedings of the Institution of Mechanical Engineers, Part H: Journal of Engineering in Medicine. 2021;235(6):676-687, https://doi:10.1177/09544119211001238

[2] Ibrahim, A. A. H., Hallak, S., & Alfayad, S. (2018), “Development of an on-board Power Pack for the hydraulic humanoid robot HYDROïD”, International Review of Mechanical Engineering (IREME),2018, 12(8), 726, https://doi.org/10.15866/ireme.v12i8.14066

[3] Ammounah, A., Ibrahim, A. A. H., Tayba, A., Alfayad, S., & Ouezdou, F. B. (2022). “Pressure Optimization of a New Hydraulic Ankle Mechanism for HYDROïD Robot”. International Review of Mechanical Engineering (IREME),2022, 16(2), 92-100, https://doi.org/10.15866/ireme.v16i2.21729

[4] D. B. Li, X. C. Li, L. Bing, Z. Y. Qiu, P. Y. Qi and W. Z. Qiao, "Simulation Analysis on flow field of profiled pipelines inside aviation hydraulic integrated block based on COMSOL," CSAA/IET International Conference on Aircraft Utility Systems (AUS 2022), Nanchang, China, 2022, pp. 656-661, https://doi.org/10.1049/icp.2022.1628.

[5] Arena M, Ambrogiani P, Raiola V, Bocchetto F, Tirelli T, Castaldo M. Design and Qualification of an Additively Manufactured Manifold for Aircraft Landing Gears Applications. Aerospace. 2023; 10(1):69, https://doi.org/10.3390/aerospace10010069.

6] D. S. Catherman, J. Tomasz Kaminski and A. Jagetia, "Atlas Humanoid Robot Control with Flexible Finite State Machines for Playing Soccer," 2020 SoutheastCon, Raleigh, NC, USA, 2020, pp. 1-7, https://doi.org/10.1109/SoutheastCon44009.2020.9368291

[7] Barasuol V, Villarreal-Magaña OA, Sangiah D, Frigerio M, Baker M, Morgan R, Medrano-Cerda GA, Caldwell DG, Semini C. “Highly-Integrated Hydraulic Smart Actuators and Smart Manifolds for High Bandwidth Force Control”. Front Robot AI. 2018 Jun 14;5:51, https://doi.org/10.3389/frobt.2018.00051

[8] Manuel Biedermann, Patrick Beutler, Mirko Meboldt, "Routing multiple flow channels for additive manufactured parts using iterative cable simulation, Additive Manufacturing", Volume 56, 2022, 102891, ISSN 2214-8604, https://doi.org/10.1016/j.addma.2022.102891

[9] Manuel Biedermann, Patrick Beutler, Mirko Meboldt, "Automated design of additive manufactured flow components with consideration of overhang constraint, Additive Manufacturing", Volume 46, 2021, 102119, ISSN 2214-8604, https://doi.org/10.1016/j.addma.2021.102119.

[10] X. Li, H. Zhou, H. Feng, S. Zhang and Y. Fu, "Design and Experiments of a Novel Hydraulic Wheel-Legged Robot (WLR)," 2018 IEEE/RSJ International Conference on Intelligent Robots and Systems (IROS), Madrid, Spain, 2018, pp. 3292-3297, https://doi.org/10.1109/IROS.2018.8594484

[11] Amrollah E, Abdellatif A, Alfayad S, Ouezdou F. "Performance enhancement of an integrated electrohydraulic actuator using dynamic modeling and optimization", Proceedings of the Institution of Mechanical Engineers, Part C: Journal of Mechanical Engineering Science. 2023;237(12):2815-2832, https://doi.org/10.1177/09544062221142404

[12] Siddique, M.A.A.; Kim, W.-S.; Kim, Y.-S.; Kim, T.-J.; Choi, C.-H.; Lee, H.-J.; Chung, S.-O.; Kim, Y.-J. Effects of Temperatures and Viscosity of the Hydraulic Oils on the Proportional Valve for a Rice Transplanter Based on PID Control Algorithm. Agriculture 2020, 10, 73, https://doi.org/10.3390/agriculture10030073

[13] Yubo Hou, Kairan Zhang, Yubin Lu, Adel Noori, "A new strategy for generating regional random fiber-reinforced polymer composite", International Journal of Mechanical Sciences, Volume 251, 2023, 108346, ISSN 0020-7403, https://doi.org/10.1016/j.ijmecsci.2023.108346

[14] A. Ibrahim, A. Ammounah, S. Alfayad, S. Tliba, F. Ouezdou, and S. Delaplace, "Hydraulic Robotic Leg for HYDROïD Robot: Modeling and Control," J. Robot. Mechatron., Vol.34 No.3, pp. 576-587, 2022, https://doi.org/10.20965/jrm.2022.p0576

[15] Kurc-Lisiecka, A., and A., Lisiecki. "Laser welding of stainless steel". Journal of Achievements in Materials and Manufacturing Engineering 98, 1 (2020): 32-40, https://doi.org/10.5604/01.3001.0014.0815

[16] Wali, A., Platt, T., Meijer, A. et al. , "Micro structuring tool steel components using Precise Electrochemical Machining (PECM)". Prod. Eng. Res. Devel. 17, 473–481 (2023), https://doi.org/10.1007/s11740-022-01167-2

[17] Lukáš Trávníček, Jan Poduška, Mario Messiha, Florian Arbeiter, Gerald Pinter, Luboš Náhlík, Pavel Hutař,"Effect of recycled material on failure by slow crack growth in multi-layer polyethylene pipes", Engineering Fracture Mechanics, Volume 289, 2023, 109423, ISSN 0013-7944, https://doi.org/10.1016/j.engfracmech.2023.109423

[18] Lupone, Federico et al. "Process Phenomena and Material Properties in Selective Laser Sintering of Polymers: A Review." Materials (Basel, Switzerland) vol. 15,1 183. 27 Dec. 2021, https://doi.org/10.3390/ma15010183

[19] K. Yogeshwaran, Shubhajit Das, "Mechanical properties of fused deposition modelling processed parts: A review", Materials Today: Proceedings, 2022, ISSN 2214-7853, https://doi.org/10.1016/j.matpr.2022.12.137

[20] A. Ahmad, M. S. Wahab, K. Kamarudin, L. W. Shun, H. Hehsan, Z. Shayfull, F. Mustafa, S. Mahmood; "Mechanical and physical properties of desktop stereolithography 3D printing materials". AIP Conf. Proc. 22 May 2023; 2530 (1): 030001, https://doi.org/10.1063/5.0121249

[21] K Srinivasa Kishore, and K Venkata Subbaiah. "Carbon Fiber and Carbon Fiber Reinforced Epoxy Composites for Automotive Applications-A Review". Journal of Advanced Research in Applied Sciences and Engineering Technology, vol. 29, no. 3, Feb. 2023, pp. 272-8, https://doi.org/10.37934/araset.29.3.272282.

[22] Nemah, Mohammed Najeh, and Hashim H. Abada. "Dynamic Model Design and Controller Development of Lower Limb Prosthesis Through Matlab Simscape Multibody Toolbox". Journal of Advanced Research in Applied Sciences and Engineering Technology, vol. 61, no. 2, Oct. 2024, pp. 110-9, https://doi.org/10.37934/araset.61.2.110119.

[23] Priatna, Edvin, et al. "Chattering Analysis of an Optimized Model Free Sliding Mode Controller for a DC Motor Speed Control". Journal of Advanced Research in Applied Sciences and Engineering Technology, vol. 51, no. 1, Sept. 2024, pp. 229-44, https://doi.org/10.37934/araset.51.1.229244.